Advanced Engineering Materials

ADVANCED ENGINEERING MATERIALS
www.aem-journal.com

RESEARCH ARTICLE OPEN ACCESS

An Inkjet-Printed Platinum-Based Temperature Sensing Element on Polyimide Substrates

Shawon Alam[1] | Thomas Kister[2] | Alexander Scholz[1] | Sophie Sauva[1] | Makara Lay[2] | Tobias Kraus[2,3] | Jasmin Aghassi-Hagmann[1]

[1]Institute of Nanotechnology (INT), Karlsruhe Institute of Technology (KIT), Karlsruhe, Germany | [2]INM – Leibniz Institute for New Materials, Saarbrücken, Germany | [3]Colloid and Interface Chemistry, Saarland University, Saarbrücken, Germany

Correspondence: Shawon Alam (shawon.alam@kit.edu)

Received: 30 June 2025 | **Revised:** 9 December 2025 | **Accepted:** 29 December 2025

Keywords: inkjet printing | linear sensitivity | nanoparticle platinum ink | polyimide substrates | resistive temperature sensors | stable temperature coefficients of resistance

ABSTRACT

In this work, we present a proof-of-concept demonstration of inkjet-printed resistive temperature sensors based on nanoparticle platinum ink on flexible polyimide substrates. The resistive temperature sensors are designed as meander structures with a target nominal resistance of 100 and 1000 Ω to be compared to conventional bulk Pt100 and Pt1000 resistors. Thermogravimetric analysis and in situ resistance measurements identified 250°C as the optimal sintering temperature, enabling sufficient solvent removal for conductive structure formation while avoiding Pt surface oxidation and polyimide substrate degradation. Electrical characterization in the 20°C–80°C range revealed a linear relationship between resistance and temperature with effective temperature coefficients of resistance (~48%/57%) and sensitivities (~72%/87%) compared to Pt100/Pt1000 standards, respectively. Mechanical testing over 400 bending cycles showed less than 1% change in electrical resistance, confirming robust flexibility. This study demonstrates the feasibility of translating nanoparticle Pt-based resistive temperature sensors into flexible and automotive sensing applications, offering low-temperature processability, stable temperature coefficients of resistance, linear sensitivity, mechanical robustness, and chemical stability across 20°C–80°C range.

1 | Introduction

Flexible temperature sensing allows for seamless and ubiquitous integration over nonconformal surfaces, which can enable novel applications in the field of wearables [1–5], biosensors [4, 6], and soft tubes [1, 6–8]. Several different types of temperature sensors such as thermistors, resistive temperature sensors (RTSs), and thermocouples are reported in literature for sensing applications [1, 6, 9, 10]. Among the reported sensors, the RTSs are widely employed because of their linear changes in electrical resistance in response to the changes in temperature [1, 4–6, 11]. Metals such as copper (Cu), gold (Au), platinum (Pt), silver (Ag), and nickel (Ni) are utilized as temperature sensing elements for RTSs [2, 6, 7, 12, 13]. However, the selection of sensing element is limited by several considerable factors such as stable temperature coefficients of resistance (TCR), linear sensitivity, resilience against oxidation, chemical stability, and manufacturing constraints [6, 14, 15].

To date, a vast majority of RTSs are reported using Ag nanoparticle ink [4, 5, 16–18] as a sensing element because of its high TCR, while a very few sensors using Pt precursor solutions ink [10] are reported that requires a relatively high sintering temperature and are not suitable for flexible substrates. However, due to the vulnerability against oxidation and large area requirement of nanoparticle Ag-based temperature sensing due to low resistivity (to reach a nominal value of 100 or 1000 Ω), the low-temperature processed nanoparticle Pt-based RTSs are preferred [15, 19, 20]. Nevertheless, the other mentioned temperature sensing elements exhibit intrinsic defects such as nonlinear variation

in electrical resistance with temperature (Ni), high oxidation rate (Ni, Cu), and high sintering temperature (Au, Cu) reported elsewhere [5, 7, 14, 19].

Pt as a temperature sensing element has drawn much attention because of its superior properties namely a sufficiently high TCR, sensitivity ($0.385\,\Omega{\cdot}°C^{-1}$ for bulk Pt100 and $3.85\,\Omega{\cdot}°C^{-1}$ for bulk Pt1000) [11, 13, 18], linear resistance changes with temperature over a broad range, and stability against oxidation owing to high melting point [6, 12, 15, 19]. Though conventional bulk Pt sensors (e.g., rigid wire-wound elements) exhibit bulk-like density and electrical conductivity [18, 20], they are resource-intensive, require high-temperature processing, and are incompatible with flexible substrates. The ability to process nanoparticle Pt at low sintering temperatures enable lightweight and cost-effective route for flexible sensing. To the best of our knowledge, there is hardly any known studies on printed nanoparticle Pt ink-based RTSs reported in the literature. Timothy et al. [21] have reported RTSs for wearable sensors using a particle-free Pt precursor ink on polyimide substrates, and a nearly linear response observed for resistance as a function of temperature between 28°C and 80°C with a sensitivity of $0.255\,\Omega{\cdot}°C^{-1}$ and a TCR of $0.000576°C^{-1}$. Therefore, this unexplored direction is particularly significant, as it enables the translation of the superior accuracy and stability of bulk Pt RTSs into low-temperature processable, lightweight, and flexible sensing elements that are scalable for automotive applications. Within this context, achieving a stable TCR and linear sensitivity remains a key challenge for accurate and reliable temperature sensing, which we address in this work.

Conventional subtractive processes such as vacuum-based physical vapor deposition (PVD), chemical vapor deposition (CVD), and photolithography are widely employed for RTS fabrication [7, 13, 22, 23]. In contrast, additive processes are advantageous in printed electronics (PE) compared to the aforementioned processes, in fulfilling the demand for the production of such sensors due to low-material waste, rapid yield, and cost-effectiveness [3, 7, 19, 24–26]. Several digital additive printing techniques including aerosol jet, electrohydrodynamic, and inkjet printing are utilized for sensor fabrication in recent times [18, 26–28]. Among the additive printing techniques, the inkjet is preferred because it offers a mask-less, noncontact, drop-on-demand, and high precision printing process that is suitable for sensor fabrication on a wide range of substrates [7, 14].

Flexible substrates such as polyethylene terephthalate (PET), polyethylene naphthalate (PEN), and polyimide (PI) are predominant in printed electronics because of their low manufacturing cost, lightweight, and flexibility [2, 4, 8, 29]. Among the flexible substrates, the PI is suitable for this work due to its superior thermal stability and mechanical flexibility, which make it particularly relevant for RTS fabrication [7, 29, 30].

In this study, we employ inkjet printing for fabricating low-temperature processed, nanoparticle Pt-based sensing element in the form of two types of RTSs, targeting bulk Pt100 and Pt1000 resistors, on PI substrates. The novelty of this work to establish a proof-of-concept route that spans nanoparticle Pt ink processing, sintering temperature optimization, standalone RTS fabrication, and electrical as well as mechanical characterization, designed to operate reliably in the 20°C–80°C range with stable TCR and linear sensitivity relevant for flexible and automotive sensing applications.

2 | Materials and Methods

2.1 | Inks and Substrates

In this study, two types of inks, namely Pt and Ag were used to fabricate the temperature sensors on PI substrates. The Pt nanoparticle (NP) ink (as a sensing element) with a concentration of 30 mg/mL was synthesized through a multistep process, initiated by the fabrication of Pt NPs employing a bottom-up approach. Initially, 360 mg of platinum (II) bis(acetylacetonate) and 1.5 g of branched polyethyleneimine (with molecular weight: 25 kDa) were introduced into a solvent mixture of 48 mL of 2-(2-ethoxyethoxy) ethanol and 12 mL of ethylene glycol. The solvent system was selected due to its capability to modulate nanoparticle size during synthesis. With an increased proportion of ethylene glycol, larger NPs are formed. To prevent rapid sedimentation in the ink, Pt NPs with an average size of approximately 20 nm were targeted. The mixture was heated to 200°C at a heating rate of 10°C per minute. This temperature was maintained for 30 min to ensure that platinum (II) bis(acetylacetonate) was fully reduced and the nanoparticles could form. Afterwards, the Pt NPs were isolated from the reaction medium via centrifugation at 10 000 rpm for 60 min. The supernatant was decanted, and the resulting Pt NPs were collected. Figure 1 shows a transmission electron microscopy (TEM) image of the Pt NPs, showing well-dispersed clusters with average particle size is in the range of ~15–25 nm.

To prepare the final ink formulation, the isolated Pt NPs were redispersed at a concentration of 30 mg/mL using an ultrasonic tip in a binary solvent mixture consisting of deionized water and ethylene glycol in a 1:1 volumetric ratio, resulting in a final solid content of approximately 2.9 wt% of Pt in the ink. The viscosity of the synthesized Pt ink was estimated to be 10 cP required for inkjet printing. However, the conductivity of Pt film, calculated from the measured sheet resistance, was $\sim 8.47 \times 10^5\,S{\cdot}m^{-1}$, corresponding to about 8.5% of bulk Pt [11, 13]. By comparison, higher concentration Pt inks (20 wt%) have been reported to reach $\sim 1.6 \times 10^6\,S{\cdot}m^{-1}$, (~17% of bulk Pt) [18, 31]. The discrepancy can be attributed to variations in Pt loading and constituents, film thickness and morphology, sheet resistance, and differences in printing as well as postprocessing parameters, all of which strongly affect the microstructure and electrical performance of the printed Pt films. However, the conductivity of Pt film

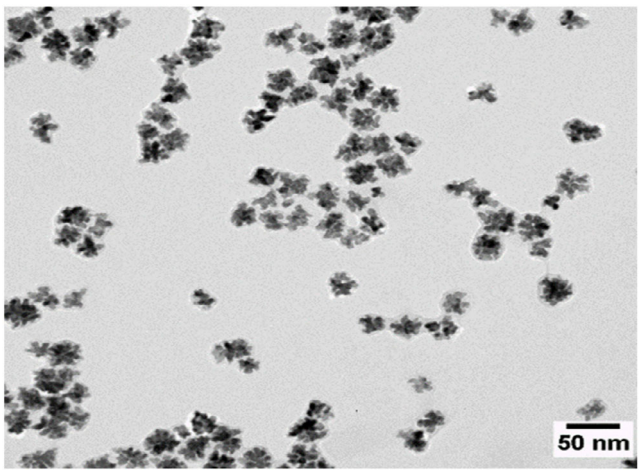

FIGURE 1 | TEM image of the synthesized Pt nanoparticles.

(~8.5% of bulk Pt) is sufficient for sensor operation, as it provides reliable current flow (e.g., ~1 mA) and stable resistance, which are essential for temperature sensing.

A commercially available Ag ink [viscosity 13 cP, Sigma–Aldrich GmbH, Germany] was used to print outer contact pads, providing stable and low-resistance electrical probing, while the Pt layer formed as the sensing element between the contact pads (Figure 2). This approach is employed to improve measurement reproducibility and sensor handling, particularly on flexible substrates. Similarly, the conductivity of the Ag is estimated to be as 0.95×10^7 S·m^{-1} (15% of bulk Ag) [13].

A PI substrate [thickness 300 µm, DuPont GmbH, Germany] was used for printing the sensing Pt elements. The PI substrate was selected because it provides light weight, high glass transition temperature up to 360°C, high stability, and flexibility that are essential for flexible sensing [4, 24, 29].

2.2 | Design of RTSs

In this work, two types of RTSs were designed using an open-source CAD software (Inkscape, GIMP and Bitmap Monochrome file format) compatible with inkjet printer. The objective was to print these RTSs on PI substrates to compare nominal resistance, TCR, and sensitivity with bulk Pt100 and Pt1000. The RTS design incorporates meander structures [4, 5, 32], where both the linewidth and the effective meander length were adjusted to achieve the required nominal resistances, while ensuring uniform temperature sensing and mechanical flexibility on polyimide substrates. The meander structure and dimensions of the RTS type A (target Pt100 resistor) and type B (target Pt1000 resistor) are depicted in Figure 2.

For RTS type A (Pt100), the meander structures had dimensions of 5 mm × 0.5 mm, whereas for RTS type B (Pt1000), the meanders were narrower (5 mm × 0.2 mm) and included a greater number of turns, resulting in a longer effective trace length and higher resistance. The Ag contact pads were identical for both types of RTSs with a dimension of about 3 mm × 3 mm.

2.3 | Fabrication of RTSs on Flexible Substrates

The Pt RTSs and Ag contact pads were printed on PI substrates by using an inkjet printer [DMP-2850, Fujifilm Corporation, Japan].

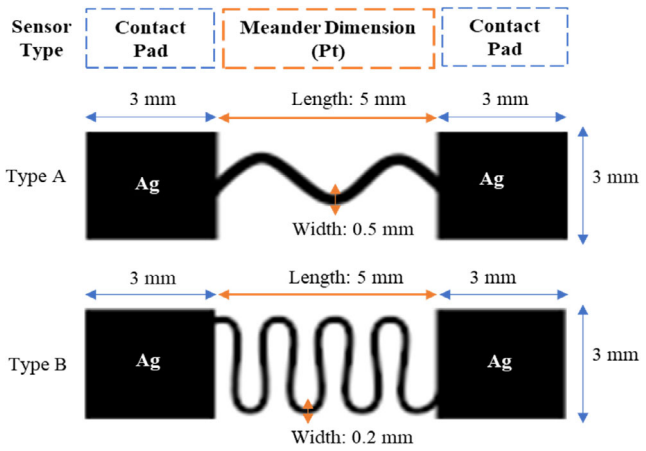

FIGURE 2 | Design of two types of RTSs.

The printer provides piezoelectric-based drop-on-demand jetting where the fluid is ejected from the printer nozzle onto the substrates by applying a voltage signal, to build up printed structures in a droplet-by-droplet approach reported elsewhere [3, 24, 33]. The success of the inkjet printing is attributed to factors such as specific viscosity (e.g., low viscous), surface tension, adhesiveness, and wetting characteristics between functional inks and PI substrates [8, 29, 34].

Prior to the printing, the PI substrates were cleaned with isopropanol to remove any residual particle or contamination on the surfaces to improve wettability and adhesion, and the inks were ultrasonicated to break large particles to prevent nozzle clogging. Table 1 summarizes the process and jetting waveform parameters optimized for inkjet printing of Pt and Ag on PI substrates, providing the necessary details to ensure reproducibility.

Upon applying the listed parameters in Table 1, Pt and Ag were printed to structure RTSs and sintered [4, 27] to achieve conductive pattern. Figure 3 illustrates the schematic printing and subsequent sintering processes of the Pt RTSs with *Ag* contact pads.

At first, Pt was printed and sintered at 250°C for 30 min, followed by Ag printing as well as sintering at 100°C for 30 min. The detailed studies on sintering the synthesized nanoparticle Pt ink are included in Section 3.2.

TABLE 1 | Inkjet printing conditions for Pt and Ag.

Printing conditions	Pt printing	*Ag* printing
Jetting voltage	35 V	36 V
Jetting frequency	2 kHz	2 kHz
Cartridge temperature	30°C	35°C
Cartridge print height	0.5 mm	0.5 mm
Substrate temperature	35°C	36°C
Drop spacing	10 µm	20 µm
Number of printed layers	2,5	2

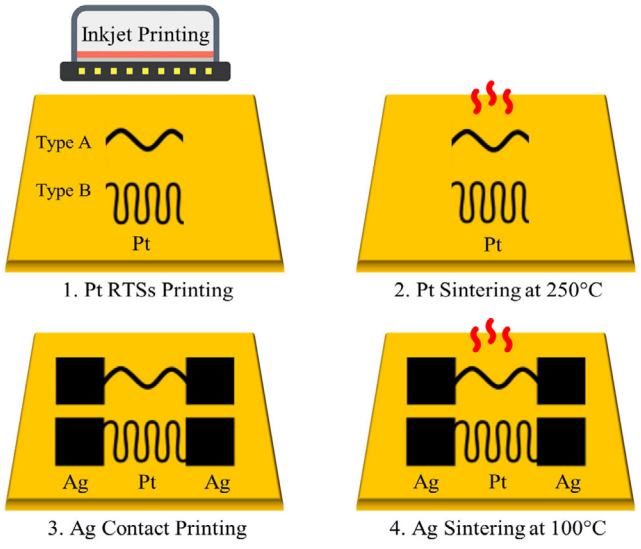

FIGURE 3 | RTSs printing and sintering steps.

3 | Results and Discussion

3.1 | Structure of RTSs

The inkjet-printed RTSs were geometrically characterized to compare the two types of design with distinct meander structures, necessary to obtain nominal resistances of 100 and 1000 Ω. Figure 4 shows the optical and atomic force microscopy (AFM) image of the Pt-based RTSs printed on PI substrates.

The designed meander layout aligns with the printed RTS structures. The sensing Pt element is in well-contact to the measuring Ag contact pads for RTS characterization as seen in Figure 4a. No significant percentage of imperfections or errors on the printed RTSs are visible from the microscopic images which means the RTSs were sufficiently sintered and the solvents were evaporated. The printed Pt RTS exhibits homogeneous surface with continuously interconnected Pt NPs regardless of their sizes as in Figure 4b, which enhances sensitivity by improving electrical conductivity, TCR, and structural stability of the sensing element.

3.2 | Sintering of RTSs

To optimize processing conditions for the printed Pt RTSs, in situ resistance measurements were performed during stepwise heating in Figure 5a. Initially, the temperature was set to 150°C and after approximately 50 min, the electrical resistance decreased from open connection (no conductivity) to around 2500 Ω. Subsequently, the temperature increased to 200°C, resulting in a further drop in resistance to approximately 1230 Ω within a few minutes, where it stabilized. A sharp decrease to ~1110 Ω was observed at 250°C, where the resistance reached a stable plateau, demonstrating that a continuous Pt structure had formed. Raising the temperature further to 300°C produced only marginal improvement (~1044 Ω) and a transient resistance increase due to Pt's intrinsic resistivity with temperature, highlighting no significant advantage beyond 250°C.

Thermogravimetric analysis (TGA) was performed to evaluate the thermal decomposition behavior of the Pt nanoparticle ink and to guide the selection of an appropriate sintering temperature. As shown in Figure 5b, the TGA curves exhibits a gradual mass loss of ~12% up to 800°C, which is attributed to the evaporation of residual solvents (deionized water and ethylene glycol binary mixture) and the removal of organic stabilizers in the ink formulation. Considering the low Pt loading of 2.9 wt%, the majority of the ink mass originates from the solvent and organic constituents, and therefore the observed relatively small mass loss is physically consistent. The dominant decomposition processes occur primarily between 150°C and 300°C, which coincides with the resistance stabilization observed in the in situ electrical measurements. The first derivative of TGA curve (inset of Figure 5b) reveals an increased mass-loss rate up to ~250°C, indicating substantial removal of volatile solvents and a significant fraction of organic stabilizers, although a limited number of residual organics may remain at this temperature. The stabilization of the curve above 300°C indicates near-complete removal of the residual organics and limited additional mass loss at higher temperatures. Although Pt is thermally stable within this temperature range, further heating may promote unwanted surface oxidation at nanoparticle interfaces. Thus, TGA results provide a clear guideline for selecting a sintering temperature that enables sufficient removal of organics while avoiding unnecessary high-temperature exposure.

Together with in situ resistance measurements, these results demonstrate that 250°C represents a practical optimum for sintering this low-solid-content (2.9 wt%) Pt nanoparticle ink. This temperature balances sufficient solvent and organic removal to achieve conductive Pt traces and stable nominal resistances, while avoiding the possibility of Pt surface oxidation and remaining within the thermal budget of polyimide substrate. Accordingly, all printed Pt RTSs in this study were sintered at 250°C for 30 min prior to electrical and mechanical characterization.

3.3 | Electrical Characterizations of RTSs

The sintered RTSs were electrically characterized at a constant relative humidity (Rh 50%) in the ambient environment. The temperature was regulated using a hotplate and varied between 20°C and 80°C with a step size of 20°C. The electrical responses of the two types of RTSs sensors are shown in Figure 6.

Both printed RTSs type A and B exhibit a linear resistance–temperature (R–T) characteristics over the investigated temperature range (Figure 6a,b), enabling linear temperature sensitivity between 20°C and 80°C. The nominal resistances of the RTSs type A varied between 87 and 162 Ω, while type B sensors resistance varied between 911 and 1814 Ω. Linear fitting yielded

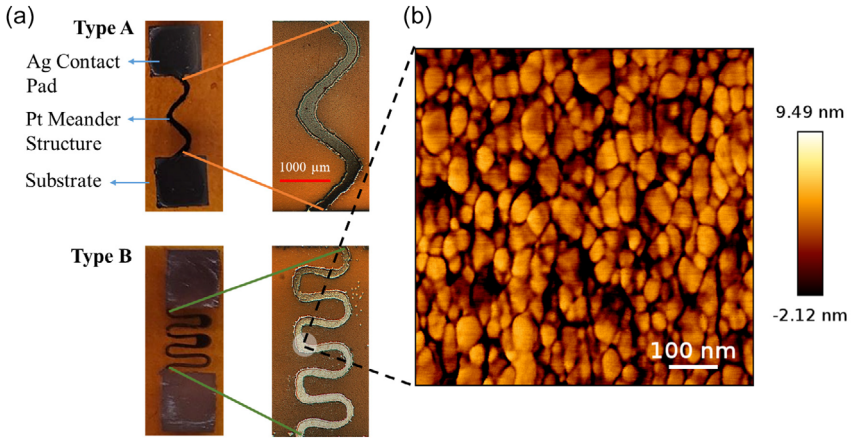

FIGURE 4 | Optical microscopy (a) and AFM image (b) of Pt RTSs on PI substrates.

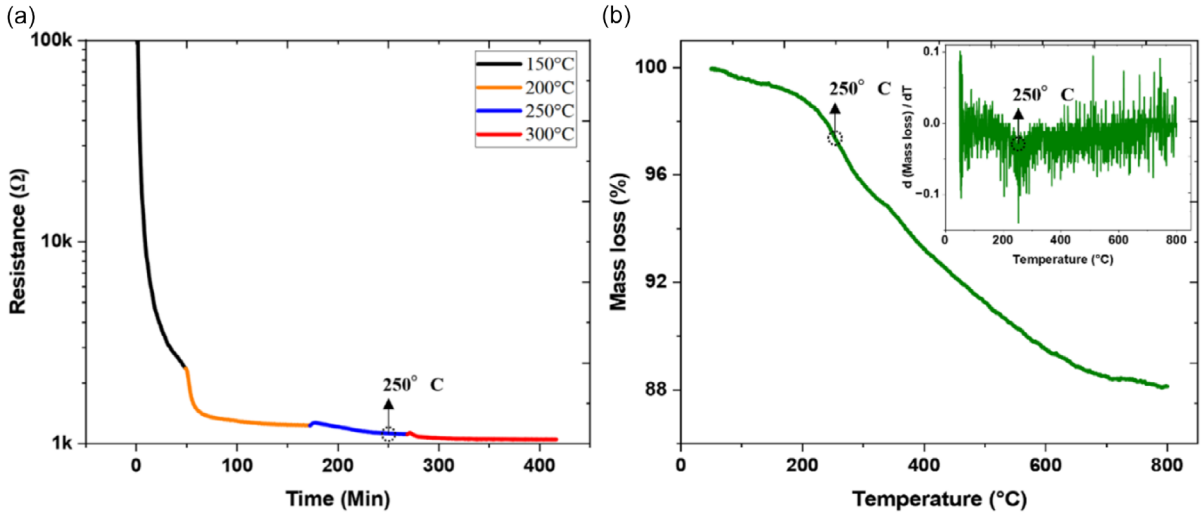

FIGURE 5 | (a) In situ resistance evolution of a printed Pt RTSs and corresponding (b) TGA analysis of the Pt ink with the derivative inset, identifying 250°C as the optimal sintering temperature.

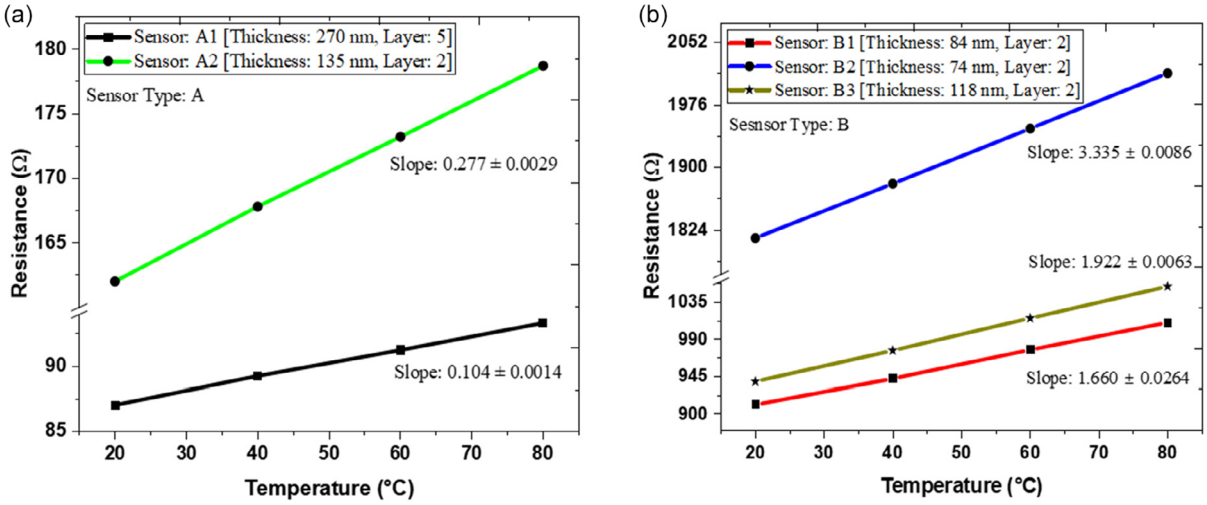

FIGURE 6 | Resistance–temperature characteristics of inkjet-printed Pt100 (type A) and Pt1000 (type B) sensors measured between 20°C and 80°C. The resistance and thickness measurements were carried out with uncertainties of ±0.1 Ω and ±5 nm, respectively.

coefficients of determination (R^2) of 0.9999 for both sensor types, confirming excellent linearity. The nominal resistances of the printed RTSs varied due to the dimension of the meander traces of sensing Pt, number of inkjet printed layers, film thickness, and printing process induced variations. The temperature dependence of the printed RTSs is described by the following equation with a small variation [4, 6, 16].

$$R(T) = R_0 \times [1 + \alpha \times (T - T_0)] \quad (1)$$

where $R(T)$ is the resistance at a measure temperature T, R_0 is the initial resistance at a defined temperature ($T_0 = 20$°C in this work), and α is the TCR of the RTSs in °C^{-1}. However, repeated temperature cycling resulted in nearly identical resistance changes, indicating negligible hysteresis in the printed Pt-based RTSs (see Figure S1). Electrical probing of sensing element with Ag contact pads introduced no discernible contact resistance, as the Ag–Pt interface showed no measurable influence on the electrical response.

For the Pt100 type sensors (type A), two printing configurations were employed to assess the effect of number of layers, including a two-layer structure (A2, ~135 nm) and a five-layer structure (A1, ~270 nm), enabling tuning of the nominal resistance toward the Pt100 range through controlled film thickness in the meander geometry of RTSs type A (5 mm × 0.5 mm). In contrast, all Pt1000 type sensors (type B, B1–B3) were printed using two layers, which were sufficient to achieve Pt1000-level nominal resistance, resulting in film thicknesses between approximately 74 and 118 nm. The relatively larger thickness variation observed among type B sensors (e.g., B2 and B3), as well as the resistance differences between B1 and B2 despite comparable thickness, is primarily attributed to the narrow meander geometry used for type B RTSs (5 mm × 0.2 mm). The narrow conductive traces are more sensitive to local variations in droplet coalescence, wetting characteristics, and sintering dynamics during inkjet printing, which directly influence meander line-width uniformity, interparticle connectivity, film densification, and hence the effective sheet resistance. Such variability inherent to nanoparticle-based metal

printing and sintering has been widely reported in the literature [35, 36]. Consequently, even when average thicknesses values are comparable, small microstructural variations inherent to nanoparticle-based inkjet printing and subsequent sintering can result in measurable resistance differences while maintaining consistent linear TCR behavior. Overall, the higher resistance of RTSs type B compared with type A is dominated by geometric scaling of the meander structures, particularly the reduced line width that increases the effective conductive path length and sheet resistance. In all cases, the meander geometry governs the nominal resistance and temperature sensitivity of the printed Pt RTSs. The Ag contact pads (~500 μm thick) ensured stable electrical contacts during thermal cycling and mechanical bending tests.

3.4 | Temperature Coefficient of Resistance and Sensitivity

The TCR and the sensitivity are the two most important parameters for RTS characterization. The TCR is described by the RTS linear changes in resistance as a function of temperature. The TCR can be mathematically derived from Equation (1) and expressed by Equation (2) [1, 6, 16].

$$\alpha_T = \frac{1}{R_0} \times \frac{R - R_0}{T - T_0} = \frac{1}{R_0} \times \frac{\Delta R}{\Delta T} \left[^\circ C^{-1}\right] \quad (2)$$

where α_T is the TCR of the RTSs in $^\circ C^{-1}$ and R denotes the resistance at maximum reference temperature ($T_{max} = 80^\circ C$ in this work). ΔR and ΔT denotes difference between resistance and temperature respectively.

The sensitivities of the RTSs are defined as a factor of resistance change per degree Celsius changes in temperature by the following equation [4, 6, 16].

$$S = \frac{R_{max} - R_0}{T_{max} - T_0} = \frac{\Delta R}{\Delta T} \left[\Omega \cdot {}^\circ C^{-1}\right] \quad (3)$$

The sensitivities of the printed RTSs are linked to TCR by Equation (4) [4, 16] and computed from the slope of Figure 6. The higher TCR value determines the higher sensitivity of the RTSs.

$$S = \alpha_T \times R_0 \left[\Omega \cdot {}^\circ C^{-1}\right] \quad (4)$$

where S is the term used to define sensitivity in $\Omega \cdot {}^\circ C^{-1}$.

The estimated TCR and sensitivity for the inkjet-printed RTSs are listed in Table 2.

The printed RTSs type A exhibit a maximum sensitivity of $0.277\ \Omega{\cdot}^\circ C^{-1}$ with a TCR of $0.00172^\circ C^{-1}$ between 20°C and 80°C, which are sufficiently higher than that of reported by Timothy et al. [21] for Pt100. To date, there is hardly any known report on Pt-based RTSs operating in the similar temperature range available in the literature. Compared with bulk Pt100 standards [11], the TCR and sensitivity of type RTSs A correspond to ~48% and ~72%, respectively. Likewise, the printed RTSs type B show a maximum sensitivity of $3.335\ \Omega{\cdot}^\circ C^{-1}$ and a TCR of $0.00205^\circ C^{-1}$ over the same range, representing ~57% and ~87% of bulk Pt1000 [37]. These results highlight the potential of inkjet-printed Pt RTSs on polyimide substrates. Reports directly comparing TCR and sensitivity of printed RTSs type B remain scarce, with most benchmarks limited to bulk Pt1000 sensors. This scarcity of data highlights the novelty of our results and their relevance as new benchmarks for printed Pt-resistive temperature sensors.

However, the data in Table 2 show that a direct comparison between the TCR and sensitivity of the inkjet-printed RTSs (type A and B) and bulk (Pt100 and Pt1000) is not straightforward, primarily due to differences in RTS nominal resistance values and meander dimensions, which directly influence $\Delta R/\Delta T$ and the effective TCR. The deviation can be attributed to factors intrinsic to the Pt composition, printing process parameters, and sintering conditions. First, the Pt ink constituents, particularly the nanoparticle distribution (e.g., 15–25 nm in size, solid content 2.9 wt%, organic residues, and inter particle distance), could play a crucial role. Nanoscale Pt particles possess high surface-to-volume ratios, leading to enhanced surface scattering and size-dependent effects that inherently reduce electrical conductivity and modify the effective TCR as well as sensitivity. Second, the Pt ink formulation and solvent residuals can also influence the microstructure after printing and sintering, which together lead to reduced film density and conductivity. The partial organic residuals persist after sintering at 250°C (confirmed by TGA) and therefore also contribute to the lower TCR observed for both RTS types (Table 2). Third, inkjet printing process variations such as droplet

TABLE 2 | Comparison of inkjet-printed Pt100 (type A) and Pt1000 (type B) RTS properties with literature, where the bulk Pt values correspond to conventional Pt wire-wound RTSs, widely used as standards.

Sensor label	Nominal resistance, $R_{20^\circ C}$, Ω	TCR, α, $^\circ C^{-1}$	Sensitivity, S, $\Omega{\cdot}^\circ C^{-1}$	Sensing range, T, °C	References
*Pt*100	107.7	0.00357	0.385	0–80	Bulk Pt100 [11]
R1	463	0.000576	0.255	28–80	Timothy et al. [21]
A1	87	0.00121	0.104	20–80	This work
A2	162	0.00172	0.277	20–80	This Work
*Pt*1000	1077.9	0.00358	3.850	0–80	Bulk Pt1000 [37]
B1	911	0.00181	1.660	20–80	This work
B2	1814	0.00184	3.335	20–80	This work
B3	938.5	0.00205	1.922	20–80	This Work

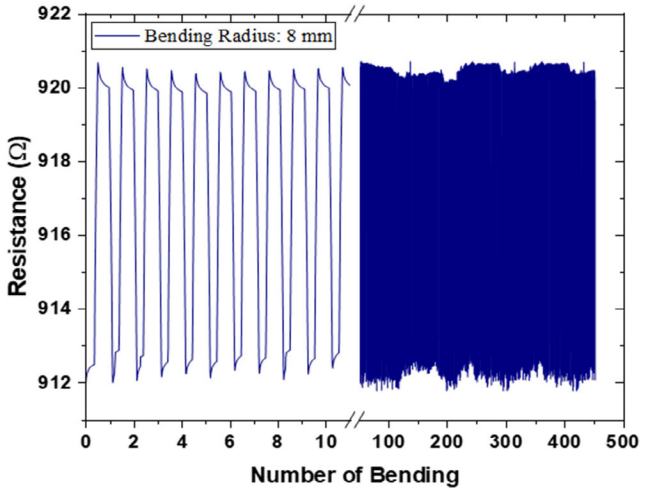

FIGURE 7 | Bending test of an inkjet printed Pt RTS on a PI substrate.

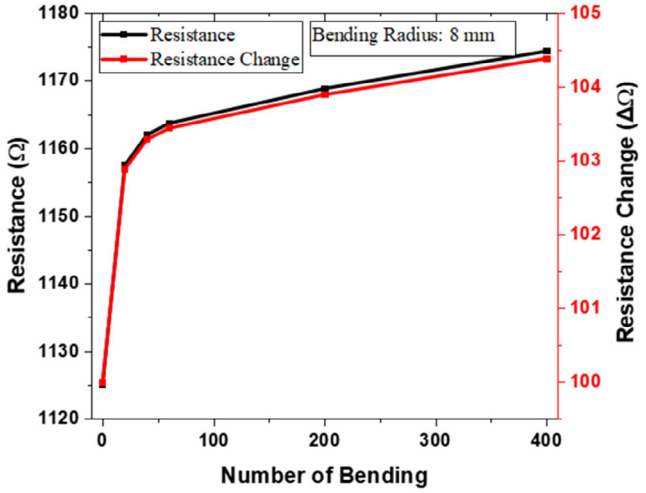

FIGURE 8 | Effect of bending cycles on the resistance of a single printed Pt-line on a PI substrate.

coalescence, layer uniformity, film thickness, and substrate wetting behavior inevitably introduce microstructural inhomogeneities that influence the meander traces resistance and TCR values. Fourth, the sintering conditions (temperature and duration) govern the extent of nanoparticle necking, grain growth, and film densification. Insufficient sintering produces discontinuous films with reduced TCR values, whereas higher-temperature sintering enhances particle connectivity and shifts the TCR closer to bulk Pt values. However, the thermal limits of polyimide substrates and oxidation of Pt restrict the maximum sintering temperature to 250°C, creating a tradeoff between stable resistance and substrate compatibility.

Despite these variations, the printed RTSs exhibit linear sensitivity over the tested temperature range (20°C–80°C) and perform effectively at a low sintering temperature of 250°C, which is advantageous for compatibility with polyimide substrates for automotive applications where integration, low-cost processing, and substrate compatibilities are prioritized over absolute equivalence with bulk Pt properties. Although the sample-set is modest in this work, all printed RTSs consistently demonstrated linear resistance–temperature characteristics and stable TCR values, confirming standalone RTS-level reproducibility within this proof-of-concept study. While this proof-of-concept demonstrates the feasibility of inkjet-printed Pt RTSs, statistical studies with larger RTS sample-set would provide access to comprehensively quantify variability, reproducibility, and process yield for rigorous benchmarking with bulk Pt and to assess scalability.

3.5 | Effect of Bending on RTSs

The bending test of the printed RTS on PI substrates was conducted to evaluate resistance changes at room temperature under mechanical stress. The RTS was attached to a cycling bending machine, which pulled the printed resistor over a spherical object with a radius of 8 mm. During bending, the resistance was continuously recorded (Figure 7).

As shown in Figure 7, the resistance increased slightly from 912 to 920 Ω during a single bending cycle (drift of <1%), while the nominal resistance remained nearly constant throughout 400 cycles. These observations confirm that the meander geometry of RTSs helps to mitigate strain localization and crack formation during bending, allowing the printed RTSs to retain mechanical stability under repeated bending.

This was further confirmed by comparing meander-type RTSs with single printed Pt-line structures (Figure 8), where the latter exhibited more pronounced resistance changes during the first 50 cycles. Beyond this initial phase, the resistance increased linearly with a small, nonzero slope, corresponding to a drift of less than

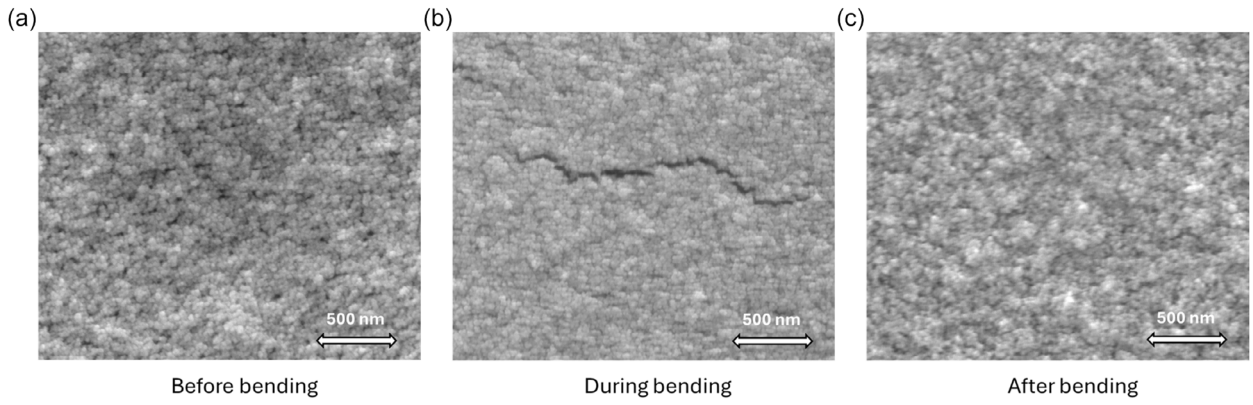

FIGURE 9 | SEM images of the Pt meander structure (a) before bending, (b) during bending, and (c) after bending.

1% of the nominal resistance between 100 and 400 cycles, confirming that the structural integrity of the printed Pt films.

In comparison, the resistance changes across the 20°C–80°C range of the printed RTSs was approximately 10%–12% (~50% of bulk change, depending on the sensor types), which is one to two orders of magnitude greater than the bending-induced drift. This demonstrates that the influence of bending-induced drift on printed RTS functionality is negligible compared to the resistance response to temperature.

To complement these electrical measurements, scanning electron microscopy (SEM) images of the Pt meander structures before and after repeated bending cycles are included in Figure 9. The postbending image reveals only localized residual microcracks that persist after strain release, rather than the transient crack opening that occurs dynamically during bending. These residual features do not significantly disrupt the meander conductive pathway, consistent with the negligible resistance drift observed during Pt RTS cyclic bending.

While extended bending tests up to 1000 cycles would provide additional long-term statistical validation, the results up to 400 cycles are sufficient to establish the mechanical robustness of the printed sensors within this proof-of-concept scope, reinforcing their suitability for flexible electronics applications.

4 | Conclusion

We reported a proof-of-concept demonstration of inkjet printed nanoparticle platinum ink based, meander-structured, resistive temperature sensors on flexible polyimide substrates. The optimal sintering temperature of 250°C revealed by thermogravimetric analysis and in situ resistance measurements, balancing sufficient solvent removal for conductive structure formation, platinum stability, and compatibility with polyimide. The printed resistive sensors closely matched the target nominal resistances of 100 Ω (type A) and 1000 Ω (type B), corresponding to bulk Pt100 and Pt1000 standards, and exhibited reproducible, linear resistance–temperature characteristics across 20°C–80°C range. The effective temperature coefficients of resistance and sensitivities were ~48%/72% of bulk Pt100 for type A, and ~57%/87% of bulk Pt1000 for type B, highlighting the influence of nanoparticle platinum ink composition, sensing meander geometry, sintering conditions, film thickness, nominal resistance values, and conductivity on sensor performance. Mechanical stability was confirmed through bending tests at an 8 mm radius, where the resistance change remained below 1% after 400 cycles. This drift is negligible compared to the ~10%–12% resistance change of the printed resistive temperature sensors over the 20°C–80°C, further supported by SEM inspection showing only minor localized microcracks without structural failure. Overall, this study establishes a material to device level proof-of-concept for inkjet-printed nanoparticle platinum-based resistive temperature sensors, demonstrating stable temperature coefficients of resistance, linear sensitivity, chemical stability, and mechanical robustness. While detailed statistical validation and extended durability testing to 1000 cycles remain a focus for future work, the present results provide a strong foundation for translating the superior properties of platinum as sensing element into low-temperature-processable, lightweight, and flexible sensing for next-generation automotive applications.

5 | Experimental Section

5.1 | Characterization of RTSs

The inkjet-printed RTSs were studied by a series of characterization techniques. An optical microscope [Hirox Digital Microscope, Tokyo, Japan] was used to verify the geometry of the printed sensors and compare with the design to ensure quality by visual inspection. The surface morphology of the RTSs were studied using atomic force microscopy (AFM) [Bruker Physik GmbH, Ettlingen, Germany] technique. The core size of the Pt NPs was measured by small-angle X-ray scattering [Xenocs SAS, Grenoble, France] and by analyzing transmission electron microscopy (TEM) [JEOL Ltd., Tokyo, Japan] micrographs. The thermogravimetric analysis (TGA) [TA Instruments TGA Q5000, New Castle, USA] was utilized to determine the thermal decomposition profile of the Pt nanoparticle ink. A hotplate in a probe station with semiconductor analyzer [Keysight Technologies, California, USA] was used to characterize the temperature sensors between 20°C and 80°C, using a step size of 20°C. Sheet resistance was measured using the four-point probe van-der-Pauw method, while the film thickness was determined with a contact surface profilometer [Veeco Dektak 6 M Surface Profiler]. The electrical conductivity (σ) of the printed Pt films was calculated from the measured sheet resistance (R_s) and the film thickness (t), using $\sigma = \frac{1}{R_s \times t}$. The printed Pt films used for conductivity estimation were fabricated using the similar dimension as the RTS type B, printed with two layers using optimized conditions described in Section 2.3, an average dried film thickness of ~80 nm, and sintered at 250°C for 30 min. An identically printed RTS type B was also used for in situ resistance measurements in Section 3.2. The experimental data of the printed RTSs were graphically represented by using Origin 2019b software. Finally, the bending test of the printed RTSs on polyimide substrate were performed using a cylindrical surface with a bending radius of 8 mm.

Acknowledgments

The authors thank the German Federal Ministry of Research, Technology, and Space (BMFTR) for the funding of this work through sensIC project. Authors (S.A., A.S., S.S., and J.A.) acknowledge funding from the Helmholtz Association under the program MSE. J.A. further acknowledges funding by the excellence cluster 3DMM2O, EXC2082 funded by German Science Foundation (DFG).

Open Access funding enabled and organized by Projekt DEAL.

Funding

This work was supported by the German Federal Ministry of Research, Technology, and Space (BMFTR), Helmholtz Association through the MSE Program, and German Research Foundation (DFG) (3DMM2O and EXC 2082).

Conflicts of Interest

The authors declare no conflicts of interest.

Data Availability Statement

The data that support the findings of this study are available from the corresponding author upon reasonable request.

References

1. M. Tursunniyaz, A. Meredith, and J. Andrews, "Aerosol Jet Printed Resistive Temperature Sensors with High Sensitivity," *Sensors and Actuators A: Physical* 364 (2023): 114777, https://doi.org/10.1016/j.sna.2023.114777.

2. Y. Su, C. Ma, J. Chen, et al., "Printable, Highly Sensitive Flexible Temperature Sensors for Human Body Temperature Monitoring: A Review," *Nanoscale Research Letters* 15, no. 1 (2020): 200, https://doi.org/10.1186/s11671-020-03428-4.

3. J. Wiklund, A. Karakoç, T. Palko, et al., "A Review on Printed Electronics: Fabrication Methods, Inks, Substrates, Applications and Environmental Impacts," *Journal of Manufacturing and Materials Processing* 5, no. 3 (2021): 89, https://doi.org/10.3390/jmmp5030089.

4. M. D. Dankoco, G. Y. Tesfay, E. Benevent, and M. Bendahan, "Temperature Sensor Realized by Inkjet Printing Process on Flexible Substrate," *Materials Science and Engineering: B* 205 (2016): 1–5, https://doi.org/10.1016/j.mseb.2015.11.003.

5. Q. J. Liew, A. S. A. Aziz, H. W. Lee, M. W. Lee, H. F. Hawari, and M. H. Md Khir, "Inkjet-Printed Flexible Temperature Sensor Based on Silver Nanoparticles Ink," *Engineering Proceedings* 2, no. 1 (2020): 3, https://doi.org/10.3390/ecsa-7-08216.

6. S. Lim and J. W. Suk, "Flexible Temperature Sensors Based on Two-Dimensional Materials for Wearable Devices," *Journal of Physics D: Applied Physics* 56, no. 6 (2023): 063001, https://doi.org/10.1088/1361-6463/acaf38.

7. X. Wang, M. Zhang, L. Zhang, J. Xu, X. Xiao, and X. Zhang, "Inkjet-Printed Flexible Sensors: From Function Materials, Manufacture Process, and Applications Perspective," *Materials Today Communications* 31 (2022): 103640, https://doi.org/10.1016/j.mtcomm.2022.103263.

8. Y. Khan, A. Thielens, S. Muin, J. Ting, C. Baumbauer, and A. C. Arias, "A New Frontier of Printed Electronics: Flexible Hybrid Electronics," *Advanced Materials* 32, no. 15 (2020): 1905279, https://doi.org/10.1002/adma.201905279.

9. J. Priest, "Temperature and its Measurement," in *Encyclopedia of Energy*, ed. C. J. Cleveland (Elsevier, 2004), 45–54, ISBN 9780121764807.

10. A. Shen, S. U. Kim, C. Bailey, M. Ma, and S. Dardona, "Direct Write Fabrication of Platinum-Based Thick-Film Resistive Temperature Detectors," *IEEE Sensors Journal* 18, no. 22 (2018): 9105–9111, https://doi.org/10.1109/JSEN.2018.2869850.

11. L. H. J. Raijmakers, D. L. Danilov, R.-A. Eichel, and P. H. L. Notten, "A Review on Various Temperature-Indication Methods for Li-Ion Batteries," *Applied Energy* 240 (2019): 918–945, https://doi.org/10.1016/j.apenergy.2019.02.078.

12. M. Zea, A. Moya, M. Fritsch, E. Ramón, R. Villa, and G. Gabriel, "Enhanced Performance Stability of Iridium Oxide-Based pH Sensors Fabricated on Rough Inkjet-Printed Platinum," *ACS Applied Materials & Interfaces* 11, no. 16 (2019): 15292–15302, https://doi.org/10.1021/acsami.9b03085.

13. K. Suganuma, *Introduction to Printed Electronics* (Springer, 2014), ISBN 9781461479070.

14. P. R. N. Childs, J. R. Greenwood, and C. A. Long, "Review of Temperature Measurement," *Review of Scientific Instruments* 71 (2000): 2959–2978, https://doi.org/10.1063/1.1305516.

15. I. A. Volkov, N. P. Simonenko, A. A. Efimov, et al., "Platinum Based Nanoparticles Produced by a Pulsed Spark Discharge as a Promising Material for Gas Sensors," *Applied Sciences* 11, no. 2 (2021): 526, https://doi.org/10.3390/app11020526.

16. A. Radwan, Y. Sui, and C. Zorman, "The Influence of Microstructure on TCR for Inkjet-Printed Resistive Temperature Detectors Fabricated Using $AgNO_3$/Ethylene-Glycol-Based Inks," *Micromachines* 15, no. 6 (2024): 749, https://doi.org/10.3390/mi15060749.

17. A. Sels and V. Subramanian, "Printed Platinum Nanoparticle Thin-Film Structures for Use in Biology and Catalysis: Synthesis, Printing, and Application Demonstration," *ACS Omega* 8, no. 2 (2023): 1799–1806, https://doi.org/10.1021/acsomega.2c04687.

18. J. Kuo, L. Yu, and E. Meng, "Micromachined Thermal Flow Sensors—A Review," *Micromachines* 3, no. 3 (2012): 550–573, https://doi.org/10.3390/mi3030550.

19. Y. Sui and C. A. Zorman, "Review—Inkjet Printing of Metal Structures for Electrochemical Sensor Applications," *Journal of the Electrochemical Society* 167, no. 3 (2020): 037571, https://doi.org/10.1149/1945-7111/ab721f.

20. R. Tao, H. Ning, J. Chen, et al., "Inkjet Printed Electrodes in Thin Film Transistors," *IEEE Journal of the Electron Devices Society* 6 (2018): 774–790, https://doi.org/10.1109/JEDS.2018.2852288.

21. T. D. Grant, J. B. Lowe, R. J. Rothwell, and A. Abdolvand, "Inkjet Printing a Platinum Temperature Sensor," in *Proceedings of the Micro and Nano Engineering Conference* (2021).

22. J. Abu-Khalaf, R. Saraireh, S. Eisa, and A. Al-Halhouli, "Experimental Characterization of Inkjet-Printed Stretchable Circuits for Wearable Sensor Applications," *Sensors* 18, no. 10 (2018): 3476, https://doi.org/10.3390/s18103476.

23. V. B. Nam and D. Lee, "Evaluation of Ni-Based Flexible Resistance Temperature Detectors Fabricated by Laser Digital Pattering," *Nanomaterials* 11, no. 3 (2021): 576, https://doi.org/10.3390/nano11030576.

24. V. Beedasy and P. J. Smith, "Printed Electronics as Prepared by Inkjet Printing," *Materials* 13, no. 3 (2020): 704, https://doi.org/10.3390/ma13030704.

25. J.-H. Ahn, H.-N. Kim, J. Y. Cho, J. H. Kim, and C.-Y. Lee, "Evaluation of Temperature Sensors for Detection of Heat Sources Using Additive Printing Method," *Sensors* 22, no. 21 (2022): 8308, https://doi.org/10.3390/s22218308.

26. A. A. Vasiliev, V. P. Kim, S. V. Tkachev, et al., "Platinum Based Material for Additive Technology of Gas Sensors," *Proceedings* 2, no. 13 (2018): 738, https://doi.org/10.3390/proceedings2130738.

27. A. Kamyshny, "Metal-Based Inkjet Inks for Printed Electronics," *Open Applied Physics Journal* 4, no. 1 (2011): 19–36, https://doi.org/10.2174/1874183501104010019.

28. S. Khan, L. Lorenzelli, and R. S. Dahiya, "Technologies for Printing Sensors and Electronics Over Large Flexible Substrates: A Review," *IEEE Sensors Journal* 15, no. 6 (2015): 3164–3185, https://doi.org/10.1109/JSEN.2014.2375203.

29. D. Maddipatla, B. B. Narakathu, and M. Atashbar, "Recent Progress in Manufacturing Techniques of Printed and Flexible Sensors: A Review," *Biosensors* 10, no. 12 (2020): 199, https://doi.org/10.3390/bios10120199.

30. K. Yan, J. Li, L. Pan, and Y. Shi, "Inkjet Printing for Flexible and Wearable Electronics," *APL Materials* 8, no. 12 (2020): 120705, https://doi.org/10.1063/5.0031669.

31. T. D. Grant, J. B. Lowe, R. J. Rothwell, and A. Abdolvand, "Inkjet Printing of High-Concentration Particle-Free Platinum Inks," *Materials & Design* 214 (2022): 110377, https://doi.org/10.1016/j.matdes.2021.110377.

32. J. Zikulnig, M. Khalifa, L. Rauter, H. Lammer, and J. Kosel, "Low-Cost Inkjet-Printed Temperature Sensors on Paper Substrate for the Integration into Natural Fiber-Reinforced Lightweight Components," *Chemosensors* 9, no. 5 (2021): 95, https://doi.org/10.3390/chemosensors9050095.

33. G. Arrabito, Y. Aleeva, R. Pezzilli, et al., "Printing ZnO Inks: From Principles to Devices," *Crystals* 10, no. 6 (2020): 449, https://doi.org/10.3390/cryst10060449.

34. S. M. F. Cruz, L. A. Rocha, and J. C. Viana, "Printing Technologies on Flexible Substrates for Printed Electronics," *Flexible Electronics* 2 (2018): 1–26, https://doi.org/10.5772/intechopen.76161.

35. J. Jäger, A. Schwenck, D. Walter, A. Bülau, K. Gläser, and A. Zimmermann, "Inkjet-Printed Temperature Sensors Characterized According to Standards," *Sensors* 22, no. 21 (2022): 8145, https://doi.org/10.3390/s22218145.

36. S. Mypati, S. R. Dhanushkodi, M. McLaren, A. Docoslis, B. A. Peppley, and D. P. J. Barz, "Optimized Inkjet-Printed Silver Nanoparticle Films: Theoretical and Experimental Investigations," *RSC Advances* 8, no. 35 (2018): 19679–19689, https://doi.org/10.1039/C8RA03627F.

37. P. Wang, X. Zhang, L. Yang, et al., "Real-Time Monitoring of Internal Temperature Evolution of the Lithium-Ion Coin Cell Battery during the Charge and Discharge Process," *Extreme Mechanics Letters* 9, no. 3 (2016): 459–466, https://doi.org/10.1016/j.eml.2016.03.013.

Supporting Information

Additional supporting information can be found online in the Supporting information section. **Supporting Fig. S1:** Resistance–temperature characteristics of inkjet-printed Pt resistive temperature sensors (a) Type A (*Pt*100) and (b) Type B (*Pt*1000), measured between 20°C and 100°C. The heating (black) and cooling (red) curves overlap, indicating negligible hysteresis and stable sensor response.